AIMS Materials Science, 3(4): 1456-1473.
DOI: 10.3934/matersci.2016.4.1456
Received: 01 September 2016
Accepted: 20 October 2016
Published: 31 October 2016

http://www.aimspress.com/journal/Materials

Research article

Nanocomposites of nitrogen-doped graphene and cobalt tungsten oxide as efficient electrode materials for application in electrochemical devices

Nirmala Kumari and Ravindra N. Singh *

Department of Chemistry, Study of Advanced centre, Institute of Science, Banaras Hindu University, Varanasi-221005, India

* **Correspondence:** Email: rnsbhu@rediffmail.com; rnsbhu@gmail.com; Tel: +91-542-6701596; Fax: +91-542-2368127.

Abstract: Nitrogen-doped graphene (N-GNS), cobalt tungsten oxide ($CoWO_4$) and their binary composites have been synthesized and their structural and electrochemical and surface properties were investigated for application as electrode materials for oxygen reduction reaction (ORR) as well as super capacitors in 1 M KOH at 25 °C. Result shows that the composite, 40%$CoWO_4$/N-GNS, has greatly enhanced capacitance as well as retention capacity, compared to its constituent compounds, N-GNS and $CoWO_4$. The ORR activity and stability of the composite are also found to be much superior to N-GNS (or $CoWO_4$) under similar conditions. The 40%$CoWO_4$/N-GNS catalyst has also exhibited reasonably good catalytic activity for oxygen evolution reaction (OER) while that the N-GNS electrode was practically inactive.

Keywords: oxygen reduction; super capacitors; nitrogen-doped graphene; nanocomposites; oxygen evolution

1. Introduction

Pt and Pt-based alloys/composites supported on carbon black have long been known as the best catalysts for the oxygen reduction reaction (ORR) in fuel cells [1]. However, their high cost and limited availability hamper the commercial application of fuel cells [2,3]. Also, Pt cathode undergoes deactivation during discharge of direct alcohol fuel cells (DAFCs) due to the crossover of alcohol

molecule from the anode to the cathode compartment through the polymer membrane [1]. To overcome these difficulties, tremendous interests have been shown during recent years toward development of low cost, efficient and stable non-precious metals and oxides [2,4–9] and metal-free electro catalysts [10,11] and are comprehensively reviewed in [12]. Recently, several heteroatom (N, B, S, P, Fe or Co)-doped carbon materials, such as carbon nanotubes (CNTs) [5,11–15], graphene [16,17], graphitic arrays [11,18] and amorphous carbon [19,20] have been found to exhibit excellent electrocatalytic performance for ORR. However, only a few novel catalysts exhibited ORR activities on a competitive level with Pt [4,11,19,21].

Graphene, a fundamental building block of the carbon based material, has been considered as the ideal low cost electrode material with large surface area (2630 $m^2 \cdot g^{-1}$), excellent electrical conductivity, high thermal and chemical stability [22]. Recently, N-doped graphene electrode materials have demonstrated excellent performances and great potentials in the field of sensor [23], Li-ion batteries [24,25], metal-air batteries [26], super capacitors [27,28], fuel cells [29,30] and so on. It is believed that graphene with suitable level of N-doping and further modifications could be promising electrode materials for varied applications.

In order to improve the ORR activity of N-doped GNS further, we have synthesized binary composites of N-doped GNS and cobalt tungsten oxide containing 5, 10, 20, 40 and 50% of the oxide by weight. Preliminary investigations have shown that the composite with 40%$CoWO_4$ is the greatest ORR active in 1 M KOH. Also, its capacitance seems to be superior to N-GNS or $CoWO_4$ alone. These results inspired us to carry out detailed investigations on the 40%$CoWO_4$/N-GNS composite material with regard to its application as ORR catalyst and also, to explore its suitability for other electrochemical applications, such as supercapacitor and oxygen evolution (EO) catalyst. Detailed results of the investigation are described in the paper.

2. Materials and Method

2.1. Preparation of Electrode Materials

2.1.1. Synthesis of GNS and N-GNS

Graphite oxide (GO) was used as the precursor in synthesis of both the graphene nano-sheets (GNS) and nitrogen doped-GNS (N-GNS). GO was prepared from graphite by the modified Hummers and Offenmans method [31]. GNS were obtained from GO as previously described [31,32]. For the preparation of N-GNS, 50 mg of GO was dispersed in 5 ml distilled water, sonicated the suspension about 1 h and to this added 30 ml ammonia (30%) and sonicated the resulting mixture, again, for 30 min. The whole content was transferred into a Teflon autoclave and heated at 220 °C for 12 h in an electric furnace. Mixture was then centrifuged and residue, so obtained, was repeatedly washed with distilled water until pH of the filtrate (i.e. washings) became neutral. It was then dried and left overnight at 100 °C [33].

2.1.2. Synthesis of $CoWO_4$

As per stoichiometry of constituent metals in the oxide, 81.1919 mg of cobalt acetate ($Co(CH_3COO)_2 \cdot 4H_2O$) was dissolved in 50 ml double distilled water and kept it at 70 °C. When the

solution attained the temperature, added slowly 50 ml sodium tungstate ($Na_2WO_4{\cdot}2H_2O$, 2.1505 $mg{\cdot}ml^{-1}$) solution under continuous stirring condition. Left the solution for 2 h under the same condition and then centrifuged, washed the precipitate thoroughly with distilled water, dried at 100 °C for overnight and finally sintered it at 500 °C for 3 h.

2.1.3. Preparation of Composites

N-GNS was prepared by hydrothermal autoclave method [33] and $CoWO_4$ was prepared by co-precipitation method [34]. Composites of N-GNS and $CoWO_4$ containing 10, 20, 40 and 50% by weight were prepared by dispersing the required quantities of N-GNS and oxide in 10 ml of double distilled water and sonicating the dispersion for 1.5 h. Subsequently, the mixture was centrifuged, washed and then dried in an oven at 100 °C for overnight.

2.1.4. Preparation of Test Electrodes

The catalyst ink was prepared, as earlier [21], by dispersing 3 mg of the catalyst powders in 600 µL of ethanol-Nafion (2:1) mixture through ultrasonication for 1 h. After that 8.4 µL of the suspension was placed over the GC disk electrode surface (0.07 cm^2), dried in air and then used for electrochemical investigations. The catalyst loading on GC was 0.6 $mg{\cdot}cm^{-2}$.

2.2. Material Characterization

2.2.1. Physiochemical

X-ray diffraction (XRD) powder patterns of the catalysts were recorded on an X-ray diffractometer (Thermo Electron) using CuK_α as the radiation source (λ = 1.541841 Å). Morphology of the catalytic films has been studied by transmission electron microscopy (TEM: TECNAI G^2 FEI). The oxidation states of metals present in the surface layer of hybrid materials were analyzed using an AMICUS-X-ray photoelectron spectrometer. All binding energy (B.E.) values were charge corrected to the C 1s signal (284.6 eV). The peak deconvolution and fittings were performed by using the XPS PEAK Version 4.1 software.

2.2.2. Electrochemical

Electrochemical studies, namely, cyclic (CV) and linear sweep voltammetries (LSV) and choronoamperometry (CA) have been carried out in a three-electrode single-compartment Pyrex glass cell using a potentiostat/galvanostat Model 273A (PARC, USA) [21]. A pure circular Pt-foil (geometrical area ≈ 8 cm^2) and SCE were used as counter and reference electrodes, respectively. The rotating disk electrode (RDE) was used as the working electrode. The disk was of GC possessing 0.07 cm^2 of surface area. The SCE electrode ($E_{calibrated}$ = 0.242 V vs. SHE) was calibrated as earlier [2,21] with respect to a reversible hydrogen electrode (RHE). The potentials mentioned in the text are given against RHE (E = −0.828 V vs. SHE) electrode only.

CV of each electrocatalyst has been carried out at a scan rate of 50 $mV{\cdot}s^{-1}$ between 0.07 and 1.17 V vs. RHE in 1 M KOH at 25 °C. Before recording the voltammogram, each electrode was

cycled for five runs at the potential scan rate of 50 $mV \cdot s^{-1}$ in 1 M KOH. CV experiments have been performed in Ar-deoxygenated and O_2-saturated 1 M KOH solutions.

LSV experiments were performed to investigate the ORR activities of hybrid electrocatalysts in O_2-saturated 1 M KOH at 25 °C. The potential range and scan rate employed were 0.07–1.17 V vs. RHE and 5 $mV \cdot s^{-1}$, respectively. To obtain O_2-saturated and deoxygenated solutions, pure O_2 and Ar gas were bubbled for 45 and 30 min, respectively. A flow of O_2 was maintained over the electrolyte during the ORR study to ensure its continued O_2 saturation.

To determine capacitance, cyclic voltammograms of the composite and N-GNS were recorded at varying scan rates (10–400 $mV \cdot s^{-1}$) in the potential region from 0.926 to 1.42 V vs. RHE in 1 M KOH. The long term cyclic performances of electrodes were also examined. For the purpose, the voltammogram was recorded between 0.926 V and 1.42 V vs. RHE at the scan rate of 200 $mV \cdot s^{-1}$ for 1000 cycles.

The oxygen evolution (OER) study has been performed by recording the LSV and Tafel curves. The potential range and scan rate employed in LSV and Tafel experiments were 1.514–1.726 V vs. RHE & 5 $mV \cdot s^{-1}$ and 1.615–1.820 V vs. RHE & 1 $mV \cdot s^{-1}$, respectively.

3. Results and Discussion

3.1. Structural Characterization

3.1.1. XRD

XRD powder patterns of GO, GNS, N-doped GNS and 40%$CoWO_4$/N-GNS recorded between 2θ = 20° and 2θ = 80°, are shown in Figure 1. In Figure 1, the diffraction peak (002) observed at 2θ = 13.24° (d = 6.67 Å) is characteristic of GO [31,35,36] and the diffraction peak (100) at 2θ = 42.54° (d = 2.1 Å) corresponds to the hexagonal structure of carbon [31].

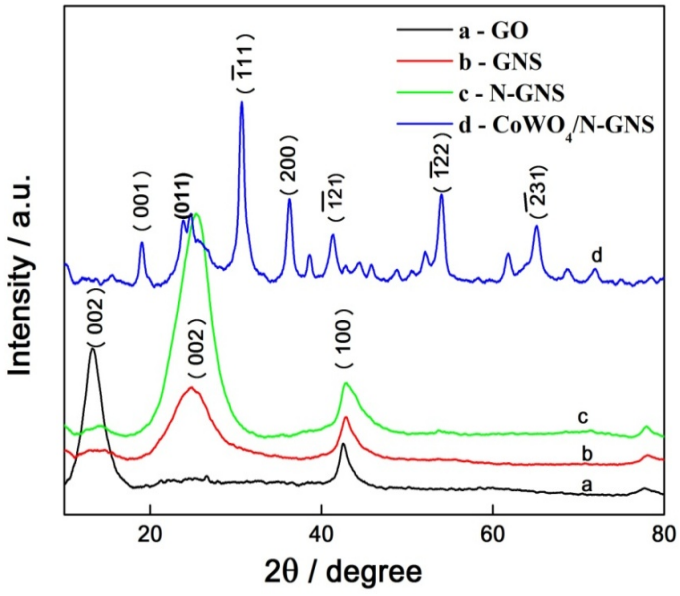

Figure 1. XRD of GO, GNS, N-GNS and 40%$CoWO_4$/N-GNS.

The observation of Figure 1 further shows that after chemical reduction of GO with $NaBH_4$, the typical diffraction peak (002) of GO shifts towards a higher angle, $2\theta = 23.06°$ (d = 3.85 Å). The displaced peak (002) looks to be broader indicating the formation of graphene nano-sheets (GNS). The XRD powder pattern of 40%$CoWO_4$/N-GNS exhibited several diffraction peaks. Among them, the prominent ones are at $2\theta = 24.72°$ (d = 3.59 Å), 30.69° (d = 2.91 Å), 36.26° (d = 2.47 Å), 41.32° (d = 2.18 Å), and 65.03° (d = 1.432 Å). These data closely match with data reported in JCPDS file 15-0867 for pure monoclinic phase of $CoWO_4$ with space group "P2/a (13)". The crystallite size of $CoWO_4$ deposited on N-GNS was 12.7 nm, which were estimated using Scherer formulae and the most intense diffraction peak.

3.1.2. Raman Spectroscopy

The Raman spectra of all the four samples, graphite oxide (GO), graphene (GNS), nitrogen-doped graphene (N-GNS) and 40%$CoWO_4$/N-GNS, shown in Figure 2, exhibit characteristics D, G and 2D bands respectively at ~1350, ~1570 and 2650 cm^{-1} [31,35,36].

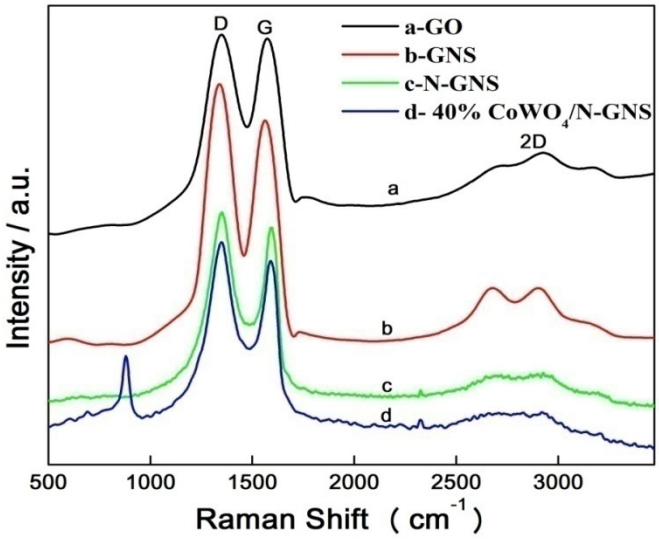

Figure 2. Raman spectra of GO, GNS, N-GNS and 40%$CoWO_4$/N-GNS.

The observation of Figure 2 shows that when GO is reduced with $NaBH_4$, a small shift in the G band takes place toward slightly lower wave number (≈7 cm^{-1}), which demonstrates that GNS is produced [39]. Further, estimates of the I_D (intensity of the D band)/I_G (intensity of the G band) ratio were found to be the highest in GNS (1.14) and the lowest in GO (1.01), value being 1.07 in N-doped GNS. The higher I_D/I_G value of GNS compared to that of GO can be attributed to the increased disorder and defects in GNS. Similarly, the level of disorder and defects also get improved when N-GNS is obtained from GO through the hydrothermal treatment with concentrated NH_3. An additional peak observed in the composite $CoWO_4$/N-GNS at 880 cm^{-1} is the characteristic peak of $CoWO_4$ [40]. The broad and less intense 2D band, shown in Figure 2, is, in fact, the second order of the D band and is characteristic of GNS. This higher order peak is used to determine the number of layers of graphene in the sample using the relationship [38,41].

$$\text{The full width at half maximum (FWHM) of 2D} = -45(1/N) + 88\ [\text{cm}^{-1}] \quad (1)$$

The above equation yields N (no. of layers) ≈ 2 which shows that the graphene contains approximately two layers. Thus, the study shows that the graphene sample used in the present study consists of 2 layers.

3.1.3. Transmission Electron Microscopy (TEM)

TEM images of N-GNS and 40%$CoWO_4$/N-GNS shown in Figure 3a–e indicate that the $CoWO_4$ nanoparticles (NPs) deposited on the N-GNS surface are nearly spherical with the average particles size of ≈14.3 nm, which is, in fact, close to the crystalline size of the oxide (12.7 nm), obtained from the XRD study. Further, the oxide NPs seem to present on the graphene surface in form of clusters (Figure 3c–e). Furthermore, the selected area electron diffraction (SAED) of the sample shown in Figure 3f reveals that the NPs are well crystallized.

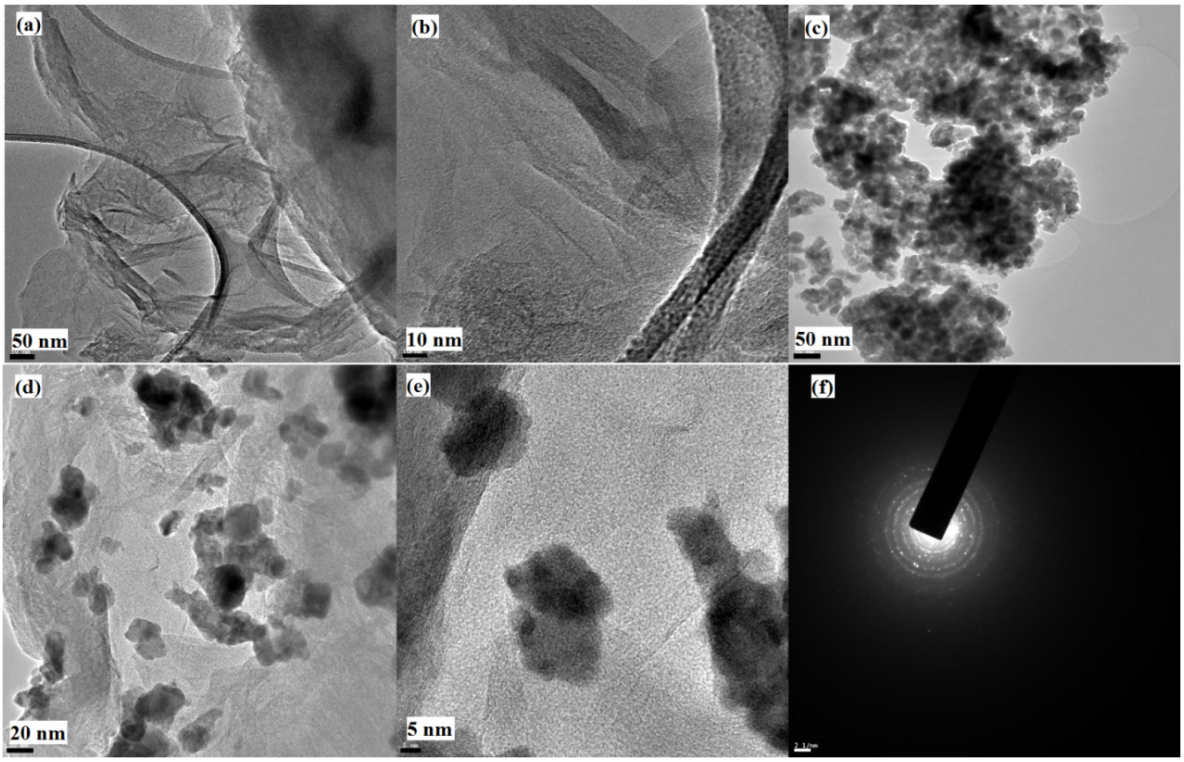

Figure 3. TEM images of N-GNS (a–b), and 40%$CoWO_4$/N-GNS (c–f).

3.1.4. X-ray Photoelectron Spectroscopy (XPS)

XPS spectra of N-doped graphene and 40%$CoWO_4$/N-GNS were recorded and core level N 1s, W 4f and Co 2p spectra are shown in Figure 4. In the N-GNS sample, only C, O, and N were detected with the content of 80%, 11.19%, and 7.98%, respectively. Deconvolution of N 1s spectrum of the sample, N-GNS (Figure 4a), yields three characteristic peaks respectively for pyridinic-N (B.E. = 398.3 eV), pyrrolic-N (B.E. = 399.6 eV) and graphitic-N (B.E. = 401.1 eV) [42]. Similar peaks were also observed for the XPS of the composite, however, they are slightly displaced toward

the higher energy (Figure 4b). Thus, results confirm the successfully chemical doping of nitrogen into the graphene structure. Estimates of distribution of N 1s into the observed three nitrogen functional groups in samples of N-GNS and composite are listed in Table 1. XPS spectra of Co 2p recorded from samples, pure $CoWO_4$ and 40%$CoWO_4$/N-GNS shown in Figure 4c look to be similar. Each spectrum exhibits four peaks: two strong (B.E.s = 780.3–781.0 & 796.6–797.4 eV) and two shake-up satellite (B.E.s = 786.4–787.4 & 802.9–804.0 eV) peaks, indicating presence of Co in the Co^{2+} oxidation state in the compound [21,34,43]. All the four peaks of Co 2p spectrum get shifted toward the higher B.E. by 0.7–1.1 eV in the case of the composite material. Similarly, the $4f_{7/2}$ (B.E. = 34.7 eV) and $4f_{5/2}$ (B.E. = 36.8 eV) photo peaks of core level W 4f spectrum from pure $CoWO_4$ sample are observed to shift toward the higher binding energy by approximately 1 eV (Figure 4d) when the same sample is present in the composite material. Thus, results show a strong interaction between N-GNS and $CoWO_4$ in the composite resulting in increase of pyridinic-N and graphitic-N and decrease of pyrrolic-N contents in the composite. Further, the XPS of W 4f of the samples, $CoWO_4$ and 40%$CoWO_4$/N-GNS shown in (Figure 4d) demonstrates that W is in oxidation state +6 [34,43].

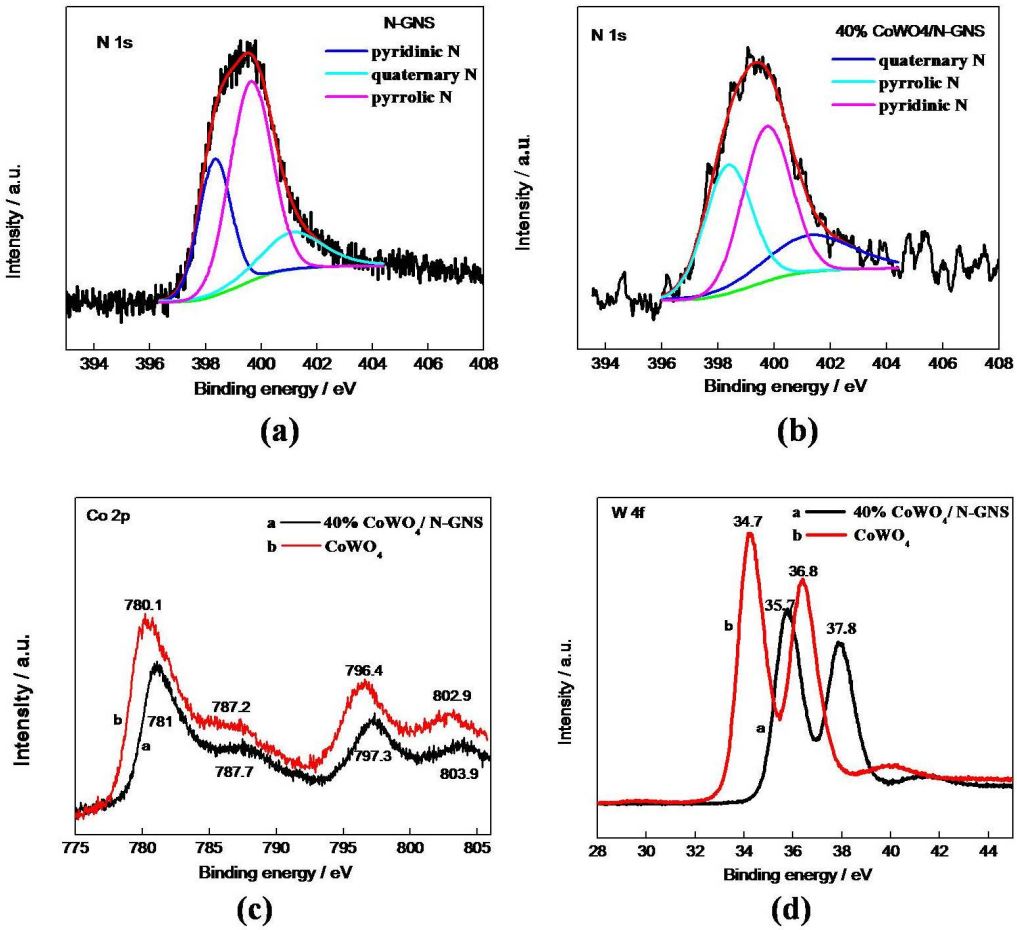

Figure 4. Core level and deconvolution XPS spectra of N 1s from samples, N-GNS (a) and $CoWO_4$/N-GNS (b); core level XPS spectra of (c) Co 2p and (d) W 4f from samples, $CoWO_4$ and 40%$CoWO_4$/N-GNS.

Table 1. Atomic distribution (N 1s) in N doped graphene and 40%$CoWO_4$/NGNS.

Samples	Pyridinic-N (at%)[a]	Pyrrolic- N (at%)[a]	Quaternary N (at%)[a]
N-GNS	28.9 (B.E. = 398.3 eV)	53.7 (B.E. = 399.6 eV)	17.3 (B.E. = 401.1 eV)
40%$CoWO_4$/NGNS	35.6 (B.E. = 398.5 eV)	43.0 (B.E. = 399.9 eV)	21.0 (B.E. = 401.1 eV)

[a] at% atomic percentage calculated from XPS result.

3.2. Electrochemical Characterization

3.2.1. Cyclic Voltammetry

CVs of $CoWO_4$, N-GNS and 40%$CoWO_4$/N-GNS recorded at 50 $mV \cdot s^{-1}$, in Ar and of the composite in O_2-saturated 1 M KOH are reproduced in Figure 5a. From observation of Figure 5a it appears that the composite material has significantly higher capacitance than those of its constituent components ($CoWO_4$ & N-GNS). It also seems to be active for ORR as is quite evident from (Figure 5b). For clarity, the ORR region of the cathodic cycle, as encircled in Figure 5b, have been expanded and are displayed in inset. To examine the possibility of this material to be use as capacitor as well as catalyst for ORR, investigations have been carried out and results, so obtained, are separately described.

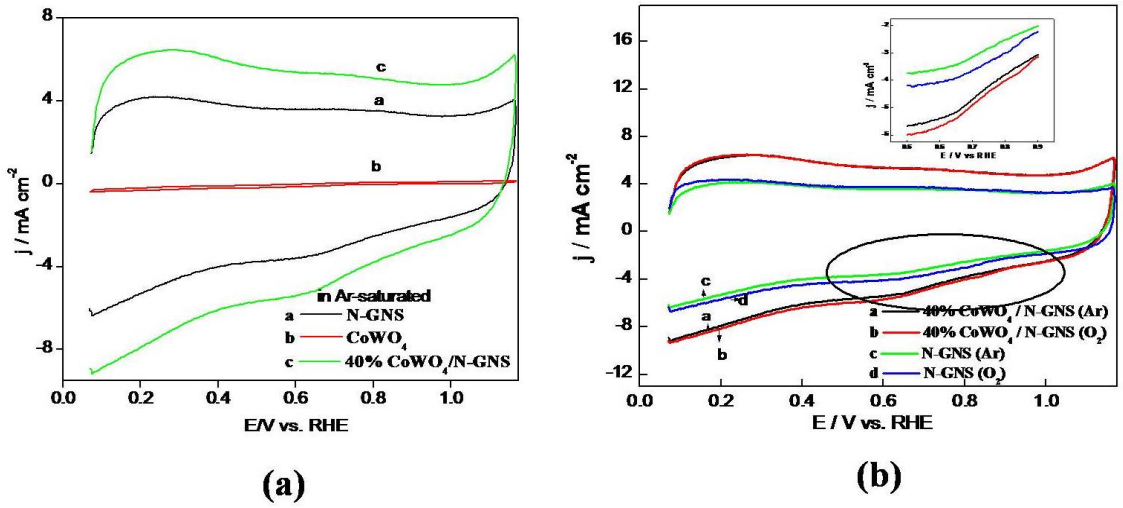

Figure 5. Cyclic voltammograms of (a) $CoWO_4$, N-GNS and 40%$CoWO_4$/N-GNS in Ar-saturated 1 M KOH (b) N-GNS and 40%$CoWO_4$/N-GNS in O_2-saturated 1 M KOH. Scan rate: 50 $mV \cdot s^{-1}$; temperature: 25 °C. The encircled part of CV curves are displayed in inset.

3.2.2. ORR Study

LSVs for N-GNS, $CoWO_4$, x%$CoWO_4$/(100−x)% N-GNS have been recorded at the constant electrode rotation of 1600 rpm in O_2-saturated 1 M KOH using the rotating disk electrode technique

(RDE) and are reproduced in (Figure 6). The scan rate and the potential region employed in the study were 5 $mV \cdot s^{-1}$ and 0.07–1.17 V vs. RHE. The catalyst loading on GC disk electrode was kept 0.6 $mg \cdot cm^{-2}$ in the ORR study. This is, in fact, the optimized loading for obtaining reproducible LSV curves.

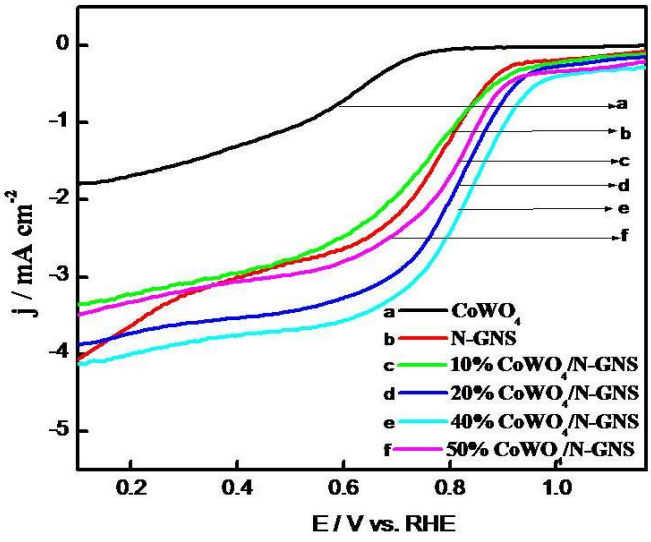

Figure 6. LSVs for $CoWO_4$, N-GNS and composites in O_2-saturated 1 M KOH. Rotation: 1600 rpm; scan rate: 5 $mV \cdot s^{-1}$; temperature: 25 °C; catalyst loading: 0.6 $mg \cdot cm^{-2}$.

Figure 6 shows that the ORR activity of $CoWO_4$ is significantly low compared to that of N-GNS. But, the ORR activities of nanocomposites of N-GNS with 20, 40 and 50% $CoWO_4$ are found to be superior to N-GNS. The onset potential for ORR has also been observed to shift toward noble side in the case of the composite electrodes. Among the $CoWO_4$/N-GNS composite electrodes investigated in the present study, the ORR activity with the composite containing 40%$CoWO_4$ is the greatest. The 10%$CoWO_4$/N-GNS electrode has more or less similar ORR activity as found with N-GNS. It was further noted that the onset (OP = 0.97 V vs. RHE) and half-wave (HWP = 0.81 V vs. RHE) potentials of our active composite electrode, $CoWO_4$/N-GNS, are very close to the commercial Pt/C catalyst (20wt% on Vulcan) (OP = 0.92 and HWP = 0.81 V vs. RHE), however, these values are higher than those recently reported for ORR on N-doped MWCNT/ $MnCo_2O_4$ (OP = 0.86 and HWP = 0.75 V vs. RHE) [44].

To evaluate the electrode kinetic parameters for ORR on N-GNS and 40%$CoWO_4$/N-GNS in O_2-saturated 1 M KOH, the LSV curves have been recorded at 5 $mV \cdot s^{-1}$ in the potential region, 0.07–1.17 V vs. RHE and at varying rotations as shown in Figure 7a–b.

Features of LSV curves shown in Figure 7 seem to be almost similar. Each curve has three distinct regions: the activation/kinetic controlled, the mixed kinetic-diffusion controlled and the mass transport-limited ones. The mixed kinetic-diffusion controlled region, 0.85–0.79 V and 0.88–0.80 V vs. RHE are chosen to obtain the kinetic information for ORR on N-GNS and composite material, respectively. At low potentials, the mass transport-limited current becomes significant where a dependence of j upon rotation rate is observed. In fact, with increasing the rotation rate, the limiting current increased due to increase in the oxygen diffusion rate from bulk to the electrode surface.

Thus, the overall measured j is, in fact, the sum of contributions of the kinetic current density, j_k and the diffusion limiting current density, j_d Both j_k and j_d can be analyzed from the RDE data using the Koutecky-Levich (K-L) equation (2) [21,45].

$$1/j = 1/j_k + 1/j_d = 1/j_k + 1/B\omega^{1/2} = 1/j_k + 1/0.2nFC_{O_2}\upsilon^{-1/6}D_{O_2}^{2/3}\omega^{1/2} \quad (2)$$

where ω is the electrode rotation rate in revolutions per minute, B is Levich constant, n is the number of electrons transferred per O_2 molecule, F is the Faraday constant (96485 $C \cdot mol^{-1}$), C_{O_2} is the concentration of O_2 in the bulk (8.4×10^{-4} $mol \cdot L^{-1}$), υ is the kinematic viscosity of the solution (1.1×10^{-2} $cm^2 \cdot s^{-1}$) and D_{O_2} is the diffusion coefficient of oxygen (1.65×10^{-5} $cm^2 \cdot s^{-1}$) [21,46].

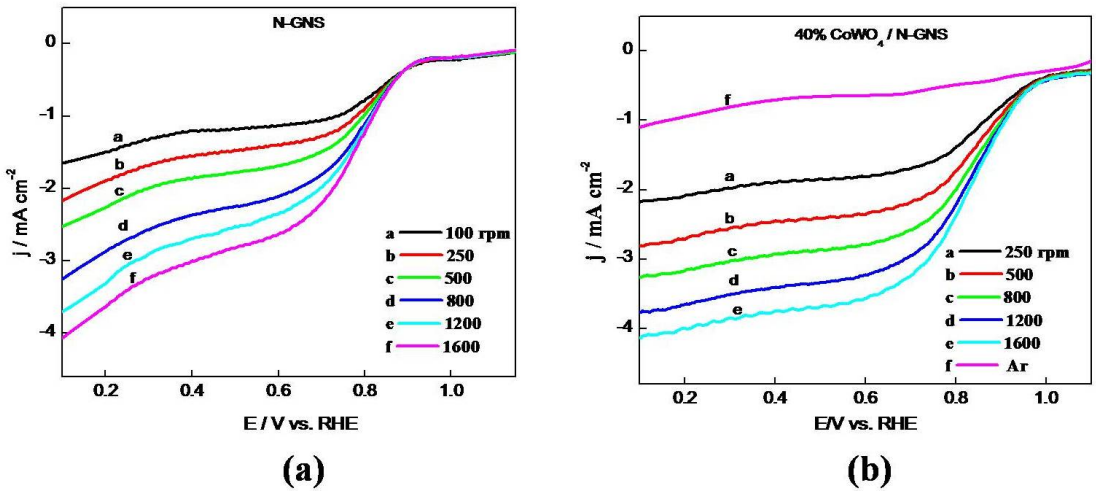

Figure 7. LSVs of N-GNS (a) and 40%$CoWO_4$/N-GNS (b) at varying rotations in O_2-saturated 1 M KOH. Scan rate: 5 $mV \cdot s^{-1}$; temperature: 25 °C; catalyst loading: 0.6 $mg \cdot cm^{-2}$.

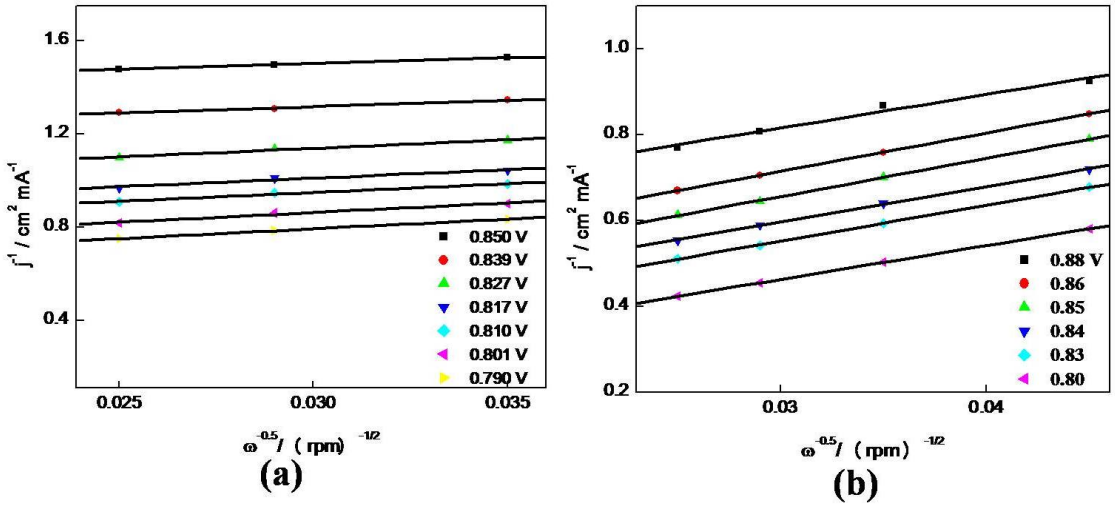

Figure 8. K-L plots for N-GNS from Figure 7(a) and for 40%$CoWO_4$/N-GNS from Figure 7(b).

From Eq. (2), the K-L plots (j^{-1} vs. $\omega^{-1/2}$) were constructed for electrodes, N-GNS and 40%$CoWO_4$/N-GNS (Figure 8a and 8b) and values of the intercept at $1/\omega^{1/2} = 0$ and the slope of each K-L curve were determined. Values of the intercept and slope, thus determined, were used to estimate values of j_k, B, j_d and n Table 2 & Table 3. In the construction of the K-L plots on composite electrode four rotations, namely 500, 800, 1200 and 1600 rpm have been considered while on N-GNS, only last three higher rotations (i.e., 800, 1200 and 1600 rpm) were considered.

The value of n is found to be 2.1–3.8 on N-GNS and 4.1–3.6 on 40%$CoWO_4$/N-GNS in the voltage range of 0.85–0.79 V vs. RHE and 0.88–0.80 V, respectively (Table 2 & Table 3). Thus, results obtained on N-GNS show that at low overpotentials, n is close to 2 and the reduction of O_2 produces HO_2^-. At the higher overpotentials n gradually increases, showing subsequent electrochemical reduction of HO_2^- to OH^-. Similar results for the ORR study on electrochemically reduced graphene oxide were also observed by Bikkarolla et al. [47]. On the other hand, the ORR on composite follows a direct $4e^-$ pathway. Recently, Bikkarolla et al. on Mn_3O_4/NrGO [48] and Seo et al. on 60%Pd/GNS and 60%Pt/GNS [49] also reported $4e^-$ pathway of ORR in 0.1 M alkaline solution. The $4e^-$ pathway of ORR on Pt has also been observed in several studies [21,50,51,52]

Table 2. The kinetic parameters for ORR on N-GNS in O_2-saturated 1 M KOH. Scan rate: 5 $mV \cdot s^{-1}$; rotation: 1600 rpm; temperature: 25 °C.

E/V	j_k/$mA \cdot cm^{-2}$	Slope (= 1/B)/$mA^{-1} \cdot cm^2 \cdot rpm^{1/2}$	j_d (= $B\omega^{1/2}$)/$mA \cdot cm^{-2}$	n = no. of electrons
0.850	0.74	4.88	8.19	2.1
0.839	0.87	5.48	7.29	2.4
0.827	1.09	7.30	5.48	3.2
0.817	1.27	7.35	5.44	3.3
0.810	1.38	7.49	5.34	3.4
0.801	1.63	8.33	4.80	3.7
0.790	1.85	8.40	4.76	3.8

Table 3. The kinetic parameters for ORR on 40%$CoWO_4$/N-GNS in O_2-saturated 1 M KOH; scan rate: 5 $mV \cdot s^{-1}$; rotation:1600 rpm; temperature: 25 °C.

E/V	j_k/$mA \cdot cm^{-2}$	Slope (= 1/B)/$mA^{-1} \cdot cm^2 \cdot rpm^{1/2}$	j_d (= $B\omega^{1/2}$)/$mA \cdot cm^{-2}$	n = no. of electrons
0.88	1.85	9.03	4.42	4.1
0.86	2.27	9.03	4.42	4.1
0.85	2.56	8.99	4.44	4.0
0.84	2.94	8.42	4.75	3.8
0.83	3.44	8.47	4.70	3.8
0.80	4.55	7.94	5.03	3.6

3.2.3. Stability Test

Chronoamperograms of the $CoWO_4$, N-GNS and composite electrodes at E = 0.39 V vs. RHE were recorded in O_2-saturated 1 M KOH for a period of 2 h and curves, so obtained, are reproduced in (Figure 9). This figure demonstrates that the stability of 40%$CoWO_4$/N-GNS is superior to N-GNS (or $CoWO_4$) under experimental conditions.

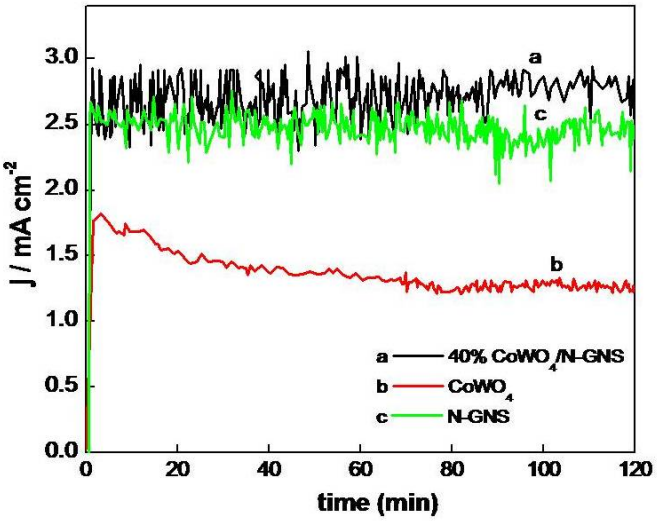

Figure 9. Chronamperograms of the $CoWO_4$, N-GNS and composite electrodes at E = 0.39 V vs. RHE in O_2-saturated 1 M KOH at 1600 rpm (25 °C).

3.2.4. Capacitance

To examine the potential application of as-prepared 40%$CoWO_4$/N-GNS nanocomposite as a super capacitor material, the cyclic voltammetry study of the composite and N-GNS has been performed at varying scan rates (10–400 $mV \cdot s^{-1}$) in 1 M KOH and results, so obtained, are shown in Figure 10. Both the electrodes exhibited approximately rectangular CV curves, indicating the double layer capacitive behavior. The observation of Figure 10 shows that the area under the anodic (or cathodic) curve at a scan rate is much higher for the composite electrode compared to pure N-GNS.

The specific capacitance ($Cs \cdot Fg^{-1}$) of the catalyst electrode at a particular scan rate was computed by determining the charge (Q/Coulomb) involved in the anodic process using the relation,

$$Cs = Q/(m\Delta E) \quad (3)$$

where, "m" is the mass of the catalytic film in "g" and "ΔE" is the potential window in "V" employed to determine cyclic voltammograms.

The capacitance of the electrode determined using relation (3) has been shown as a function of scan rate in Figure 11a. This figure demonstrates that the capacitance of the composite, $CoWO_4$/N-GNS is much higher than that of N-GNS. Further, the specific capacitance is maximum at the lowest scan rate in case of both electrodes. For instance, at 10 $mV \cdot s^{-1}$, estimates of Cs were 41.88 and 34.65 Fg^{-1} for electrodes, 40%$CoWO_4$/N-GNS and N-GNS, respectively. The enhanced specific

capacitance can be ascribed to the decrease in aggregation of N-doped graphene nano-sheets and better dispersion of the oxide nano-particles on the surface of N-GNS [40].

The long term cyclic performances of the composite and N-GNS were also examined in this study by repeating the CV between 0.926 V to 1.42 V (vs. RHE) at a scan rate of 200 $mV \cdot s^{-1}$ for 1000 cycles. The specific capacitance of N-GNS and composite electrodes as a function of cycle number is presented in Figure 11b. This figure clearly demonstrates that the composite electrode has better stability than N-GNS. For instance, over 1000 cycles at the scan rate of 200 $mV \cdot s^{-1}$, estimate of the capacity retention is 89% in the case of the composite electrode while it is only 73% in the case of N-GNS. This result indicates that the 40%$CoWO_4$/N-GNS electrode is highly durable for electrochemical capacitor applications in 1 M KOH.

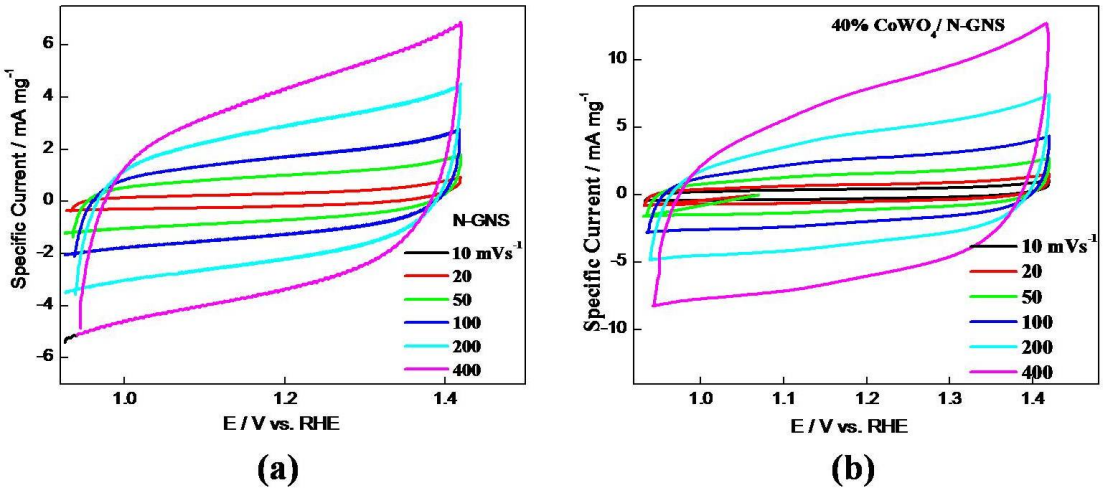

Figure 10. Cyclic voltammograms of N-GNS and 40%$CoWO_4$/N-GNS catalysts at varying scan rates in Ar-saturated 1 M KOH.

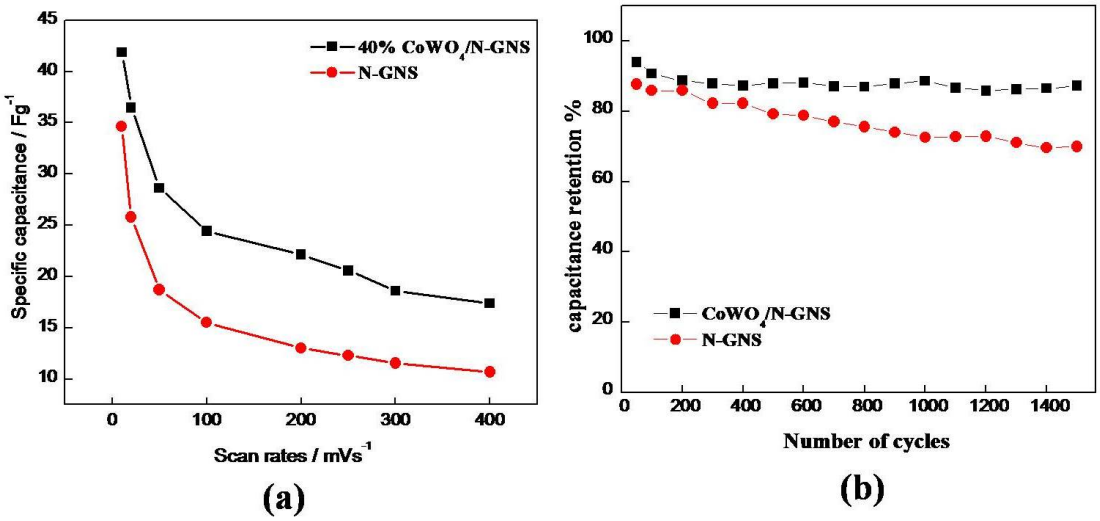

Figure 11. (a) Plots of the specific capacitance as function of scan rate from (Figure 10a and 10b) and (b) capacitance retention as a function of number of cycles.

3.2.5. Oxygen Evolution (OER)

The activities of N-GNS and composite electrode toward O_2 evolution reaction (OER) have also been examined in 1 M KOH at 25 °C and results are shown in Figure 12. This figure shows that the composite electrode is OER active also. The N-GNS electrode is practically OER inactive one. The anodic Tafel plot (E vs. log j) for OER at the active electrode was also recorded at the scan rate of 1 $mV \cdot s^{-1}$ in the potential region from 1.615 to 1.820 V vs. RHE in 1 M KOH and the curve, so obtained, is reproduced in Figure 13. Estimates of the Tafel slope (b) and the overpotential (η_{O_2}) at the current density of 10 $mA \cdot cm^{-2}$ were 62 ± 3 mV and 418 ± 1 mV, respectively; two electrodes of the composite were used for the investigation.

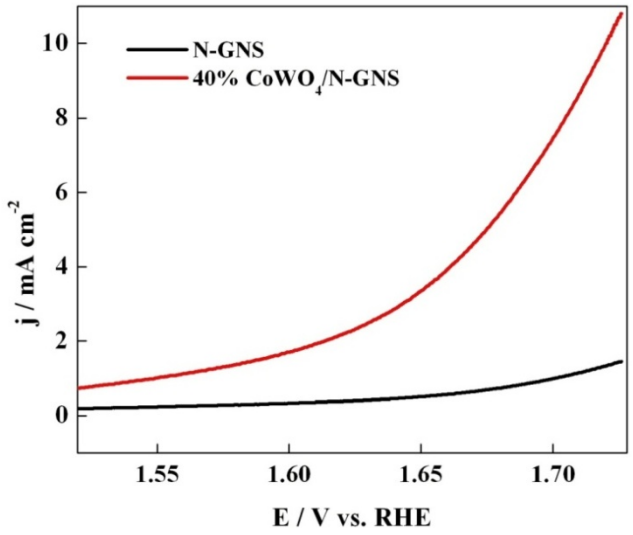

Figure 12. LSV curves for N-GNS and 40%$CoWO_4$/N-GNS at the scan rate of 5 $mV \cdot s^{-1}$ in 1 M KOH at 25 °C.

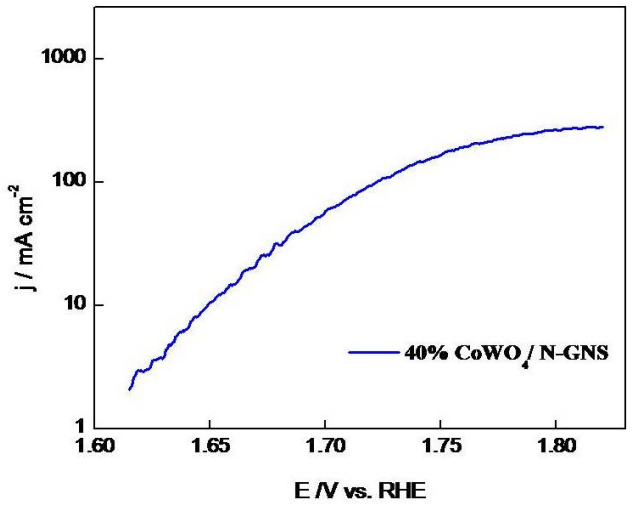

Figure 13. Anodic Tafel polarization curve for 40%$CoWO_4$/N-GNS at the scan rate of 1 $mV \cdot s^{-1}$ in 1 M KOH at 25 °C.

4. Conclusion

The study has indicated that the composite of N-GNS with 40%$CoWO_4$ has greatly enhanced capacitance as well as ORR activity compared to its constituent compounds, N-GNS and $CoWO_4$ in 1 M KOH. The composite electrode is OER active, on the contrary, the N-GNS electrode is OER inactive one. A significant increase in catalytic activity of the composite towards ORR can be attributed to the existence of a strong interaction between N-GNS and $CoWO_4$ in the composite resulting in increase of pyridinic-N and graphitic-N and decrease of pyrrolic-N contents in the composite. The stability of novel composite material is also superior to N-GNS. Thus, the 40%$CoWO_4$/N-GNS can be used at a good bi-functional oxygen electrode material. It has also good cyclic stability for potential applications as super capacitor electrodes. So, there seems possibility of developing promising materials with suitable combinations of transition metal oxides and N-GNS for use in high performance super capacitors as well as fuel cells.

Acknowledgements

The authors acknowledge the support received by the University Grants Commission (F.No.18-1/2011BSR) & (UGC-BSR/RFSMS/434), Government of India to carry out the research work.

Conflict of Interest

The authors declare that there is no conflict of interest regarding the publication of this manuscript.

References

1. Singh RN, Awasthi R, Sharma CS (2014) Review: An overview of recent development of platinum-based cathode materials for direct methanol fuel Cells. *Int J Electrochem Sci* 9: 5607–5639.
2. Liang Y, Li Y, Wang H, et al. (2011) Co_3O_4 nanocrystals on graphene as a synergistic catalyst for oxygen reduction reaction. *Nat Mater* 10: 780–786.
3. Singh RN, Singh A (2009) Electrocatalytic activity of binary and ternary composite film of Pd, MWCNT, and Ni for ethanol electrooxidation in alkaline solutions. *Carbon* 47: 271–278.
4. Wu G, More KL, Johnston CM, et al. (2011) High-performance electrocatalysts for oxygen reduction derived from polyaniline, iron, and cobalt. *Science* 332: 443–447.
5. Wu ZS, Yang S, Sun Y (2012) 3D Nitrogen-doped graphene aerogel supported Fe_3O_4 nanoparticles as efficient electrocatalysts for the oxygen reduction Reaction. *J Am Chem Soc* 134: 9082–9085.
6. Hamdani M, Singh RN, Chartier P (2010) Co_3O_4 and Co-based spinel oxides bifunctional oxygen electrodes. *Int J Electrochem Sci* 5: 556–577.
7. Singh RN, Lal B, Malviya M (2004) Electrocatalytic activity of electrodeposited composite films of polypyrrole and $CoFe_2O_4$ nanoparticles towards oxygen reduction reaction. *Electrochim Acta* 49: 4605–4612.

8. Wu G, Chung HT, Nelson M, et al. (2011) Graphene-riched Co_9S_8-N-C non-precious metal catalyst for oxygen reduction in alkaline media. *ECS Trans* 41: 1709–1717.
9. Singh RN, Malviya M, et al. (2007) Polypyrrole and $La_{1-x}Sr_xMnO_3$ ($0 \leq x \leq 0.4$) composite electrodes for electroreduction of oxygen in alkaline medium. *Electrochim Acta* 52: 4264–4271.
10. Li Y, Zhou W, Wang H, et al. (2012) An oxygen reduction electrocatalyst based on carbon nanotube-graphene complexes. *Nat Nanotechnol* 7: 394–400.
11. Gong K, Du F, Xia Z, et al. (2009) Nitrogen-doped carbon nanotube arrays with high electrocatalytic activity for oxygen reduction. *Science* 323: 760–764.
12. Liu M, Zhang R, Chen W (2014) Graphene-supported nanoelectrocatalysts for fuel cells: synthesis, properties, and applications. *Chem Rev* 114: 5117−5160.
13. Choi CH, Park SH, Woo SI (2012) Binary and ternary doping of nitrogen, boron, and phosphorus into carbon for enhancing electrochemical oxygen reduction activity. *ACS Nano* 6: 7084−7091.
14. Wang S, Iyyamperumal E, Roy A, et al. (2011) Vertically aligned BCN nanotubes as efficient metal-free electrocatalysts for oxygen reduction reaction: a synergetic effect by Co-doping with boron and nitrogen. *Angew Chem Int Edit* 50: 11756–11760.
15. Ma G, Jia R, Zhao J, et al. (2011) Nitrogen-doped hollow carbon nanoparticles with excellent oxygen reduction performances and their electrocatalytic kinetics. *J Phys Chem C* 115: 25148–25154.
16. Geng D, Chen Y, Chen Y, et al. (2011) High oxygen-reduction activity and durability of nitrogen-doped graphene. *Energy Environ Sci* 4: 760–764.
17. Li Y, Zhao Y, Cheng H, et al. (2012) Nitrogen-doped graphene quantum dots with oxygen-rich functional groups. *J Am Chem Soc* 134: 15–18.
18. Liang J, Zheng Y, Chen J, et al. (2012) Facile oxygen reduction on a three-dimensionally ordered macroporous graphitic C_3N_4/carbon composite electrocatalyst. *Angew Chem Int Edit* 51: 3892–3896.
19. Xia W, Masa J, Bron M, et al. (2011) Highly active metal-free nitrogen-containing carbon catalysts for oxygen reduction synthesized by thermal treatment of polypyridine-carbon black mixtures. *Electrochem Commun* 13: 593–596.
20. Yang W, Fellinger TP, Antoniett M (2011) Efficient metal-free oxygen reduction in alkaline medium on high-surface-area mesoporous nitrogen-doped carbons made from ionic liquids and nucleobases. *J Am Chem Soc* 133: 206–209.
21. Sharma CS, Awasthi R, Singh RN, et al. (2013) Graphene-cobaltite-Pd hybrid materials for use as efficient bifunctional electrocatalysts in alkaline direct methanol fuel cells. *Phys Chem Chem Phys* 15: 20333–20344.
22. Geim AK (2009) Graphene: status and prospects. *Science* 324: 1530–1534.
23. Wang Y, Shao Y, Matson DW, et al. (2010) Nitrogen-doped graphene and its application in electrochemical biosensing. *ACS Nano* 4: 1790–1798.
24. Li D, Shi D, Chen Z, et al. (2013) Enhanced rate performance of cobalt oxide/nitrogen doped graphene composite for lithium ion batteries. *RSC Adv* 3: 5003–5008.
25. Wu G, Mack NH, Gao W, et al. (2012) Nitrogen-doped graphene-rich catalysts derived from heteroatom polymers for oxygen reduction in nonaqueous lithium-O_2 battery cathodes. *ACS Nano* 6: 9764–9776.
26. Higgins D, Chen Z, Lee DU, et al. (2013) Activated and nitrogen-doped exfoliated graphene as air electrodes for metal-air battery applications. *J Mater Chem A* 1: 2639–2645.

27. Hassan FM, Chabot V, Li J, et al. (2013) Pyrrolic-structure enriched nitrogen doped graphene for highly efficient next generation supercapacitors. *J Mater Chem A* 1: 2904–2912.
28. Wu ZS, Winter A, Chen L, et al. (2012) Three-dimensional nitrogen and boron co-doped graphene for high-performance all-solid-state supercapacitors. *Adv Mater* 24: 5130–5135.
29. Qu L, Liu Y, Baek JB, et al. (2010) Nitrogen-doped graphene as efficient metal-free electrocatalyst for oxygen reduction in fuel cells. *ACS Nano* 4: 1321–1326.
30. Li Q, Zhang S, Dai L, et al. (2012) Nitrogen-doped colloidal graphene quantum dots and their size-dependent electrocatalytic activity for the oxygen reduction reaction. *J Am Chem Soc* 134: 18932–18935.
31. Singh RN, Awasthi R (2011) Graphene support for enhanced electrocatalytic activity of Pd for alcohol oxidation. *Catal Sci Technol* 1: 778–783.
32. Cote LJ, Kim F, Huang J (2009) Langmuir-Blodgett assembly of graphite oxide single layers. *J Am Chem Soc* 131: 1043–1049.
33. Feng L, Yang L, Huang Z, et al. (2013) Enhancing electrocatalytic oxygen reduction on nitrogen-doped graphene by active sites implantation. *Sci Rep* 3: 442–455.
34. Srirapu VKVP, Kumar A, Srivastava P, et al. (2016) Nanosized $CoWO_4$ and $NiWO_4$ as efficient oxygen-evolving electrocatalysts. *Electrochim Acta* 209: 75–84.
35. Li Y, Gao W, Ci L, et al. (2010) Catalytic performance of Pt nanoparticles on reduced graphene oxide for methanol electro-oxidation. *Carbon* 48: 1124–1130.
36. Jeong HK, Lee YP, Lahaye RJWE, et al. (2008) Evidence of graphitic AB stacking order of graphite oxides. *J Am Chem Soc* 130: 1362–1366.
37. Niu JJ, Wang JN (2008) Activated carbon nanotubes-supported catalyst in fuel cells. *Electrochim Acta* 53: 8058–8063.
38. Dervishi E, Li Z, Watanabe F, et al. (2009) Large-scale graphene production by RF-cCVD method. *Chem Commun* 27: 4061–4063.
39. Choi SM, Seo MH, Kim HJ, et al. (2011) Synthesis of surface-functionalized graphene nano sheets with high Pt-loadings and their applications to methanol electrooxidation. *Carbon* 49: 904–909.
40. Xu X, Shen J, Li N, et al. (2014) Facile synthesis of reduced graphene oxide/$CoWO_4$ nanaocomposites with enhanced electrochemical performances for supercapacitors. *Electrochim Acta* 150: 23–34.
41. Vericat C, Vela ME, Salvarezza RC (2005) Self-assembled monolayers of alkanethiols on Au (111): surface structures, defects and dynamics. *Phys Chem Chem Phys* 7: 3258–3268.
42. Sheng ZH, Shao L, Chen JJ, et al. (2011) Catalyst-free synthesis of nitrogen doped graphene via thermal annealing graphite oxide with melamine and its excellent electrocatalysis. *ACS Nano* 5: 4350–4358.
43. Rajagopal S, Nataraj D, Khyzhun OY, et al. (2010) Hydrothermal synthesis and electronic properties of $FeWO_4$ and $CoWO_4$ nanostructures. *J Alloys Compd* 493: 340–345.
44. Yuvaraj S, Vignesh A, Shanmugam S, et al. (2016) Nitrogen-doped multi-walled carbon nanotubes-$MnCo_2O_4$ microsphere as electrocatalyst for efficient oxygen reduction reaction. *Int J Hydrogen Energ* 41: 15199–15207.
45. Borja-Arco E, Castellanos RH, Uribe-Godínez J, et al. (2009) Osmium-ruthenium carbonyl clusters as methanol tolerant electrocatalysts for oxygen reduction. *J Power Sources* 188: 387–396.

46. Lee CL, Chiou HP, Syu CM, et al. (2011) Displacement triangular Ag/Pd nanoplate as methanol-tolerant electrocatalyst in oxygen reduction reaction. *Int J Hydrogen Energ* 36: 12706–12714.
47. Bikkarolla SK, Cumpson P, Joseph P, et al. (2014) Oxygen reduction reaction by electrochemically reduced graphene oxide. *Faraday Discuss* 17: 415–428.
48. Bikkarolla SK, Yu F, Zhou W, et al. (2014) A three-dimensional Mn_3O_4 network supported on a nitrogenated graphene electrocatalyst for efficient oxygen reduction reaction in alkaline Media. *J Mater Chem A* 2: 14493–14501.
49. Seo MH, Choi SM, Kim HJ, et al. (2011) The graphene-supported Pd and Pt catalysts for highly active oxygen reduction reaction in an alkaline condition. *Electrochem Commun* 13: 182–185.
50. Adzic R (1998) Recent advances in the kinetics of oxygen reduction, in Electrocatalysis, ed. Lipkowski J and Ross PN, New York, Wiley-VCH.
51. Sarapuu A, Kasikov A, Laaksonen T, et al. (2008) Electrochemical reduction of oxygen on thin-film Pt electrodes in acid solutions. *Electrochim Acta* 53: 5873–5880.
52. Li B, Prakash J (2009) Oxygen reduction reaction on carbon supported Palladium-Nickel alloys in alkaline media. *Electrochemistry Commun* 11: 1162–1165.

AIMS Press